PCCP

www.rsc.org/pccp

PAPER

In situ coarsening study of inverse micelle-prepared Pt nanoparticles supported on γ-Al$_2$O$_3$: pretreatment and environmental effects†

J. Matos,[a] L. K. Ono,[a] F. Behafarid,[a] J. R. Croy,[a] S. Mostafa,[a] A. T. DeLaRiva,[b] A. K. Datye,[b] A. I. Frenkel[c] and B. Roldan Cuenya*[a]

The thermal stability of inverse micelle prepared Pt nanoparticles (NPs) supported on nanocrystalline γ-Al$_2$O$_3$ was monitored *in situ* under different chemical environments (H$_2$, O$_2$, H$_2$O) *via* extended X-ray absorption fine-structure spectroscopy (EXAFS) and *ex situ via* scanning transmission electron microscopy (STEM). Drastic differences in the stability of identically synthesized NP samples were observed upon exposure to two different pre-treatments. In particular, exposure to O$_2$ at 400 °C before high temperature annealing in H$_2$ (800 °C) was found to result in the stabilization of the inverse micelle prepared Pt NPs, reaching a maximum overall size after moderate coarsening of ∼1 nm. Interestingly, when an analogous sample was pre-treated in H$_2$ at ∼400 °C, a final size of ∼5 nm was reached at 800 °C. The beneficial role of oxygen in the stabilization of small Pt NPs was also observed *in situ* during annealing treatments in O$_2$ at 450 °C for several hours. In particular, while NPs of 0.5 ± 0.1 nm initial average size did not display any significant sintering (0.6 ± 0.2 nm final size), an analogous thermal treatment in hydrogen leads to NP coarsening (1.2 ± 0.3 nm). The same sample pre-dosed and annealed in an atmosphere containing water only displayed moderate sintering (0.8 ± 0.3 nm). Our data suggest that PtO$_x$ species, possibly modifying the NP/support interface, play a role in the stabilization of small Pt NPs. Our study reveals the enhanced thermal stability of inverse micelle prepared Pt NPs and the importance of the sample pre-treatment and annealing environment in the minimization of undesired sintering processes affecting the catalytic performance of nanosized particles.

1. Introduction

The crucial role that the nanoparticle (NP) size plays in a variety of technological applications of nanomaterials in the fields of nanoelectronics, optics, sensing, and catalysis has become common knowledge.[1–7] In particular, due to the increased surface to volume ratio obtained with decreasing NP size and the availability of an increasing fraction of low-coordinated atoms on the NP surface, enhanced catalytic performance has been generally reported with decreasing NP size.[8–15] Furthermore, the NP size was also shown to influence the binding of adsorbates[16,17] and selectivity of NP catalysts.[18–22] Sintering is a major factor contributing to the decrease in the reactivity of NPs used in catalytic converters[23] and fuel cells.[24] Therefore, designing NP-support systems that ensure the stability of the NPs under reaction conditions, *e.g.*, under a

given chemical environment and at high temperature, is essential in order to maintain their catalytic performance and lifetime in an industrial setting.[25] A variety of approaches have been used in the past in order to stabilize NPs, including their confinement in mesoporous matrices, encapsulation by ligands, and chemical redispersion pre-treatments.[1,15,26–33] Nevertheless, extreme caution must be taken when using some of the former approaches in order not to compromise active reaction sites due to residual contamination from the stabilizing agents, or to the limited accessibility of certain reactants to the NPs.

Although a number of studies have been dedicated to monitoring NP formation and stability before and after reaction or after a given thermal treatment,[25,34–41] fewer *in situ* real-time investigations are available.[42–45] Furthermore, despite the fact that in industrially relevant catalytic combustion processes NP sintering occurs at elevated temperatures (> 750 °C),[46–50] most of the *in situ* studies published to date describe a much lower temperature regime,[51] which is due in part to intrinsic limitations of the experimental techniques used. The present work describes the effect of the NP synthesis method, pre-treatment and annealing environment on the thermal stability and coarsening behavior of inverse micelle

a Department of Physics, University of Central Florida, Orlando, Florida 32816, USA. E-mail: roldan@ucf.edu
b Department of Chemical and Nuclear Engineering, University of New Mexico, Albuquerque, NM 87131, USA
c Department of Physics, Yeshiva University, New York, New York 10016, USA

† Electronic supplementary information (ESI) available. See DOI: 10.1039/c2cp41339f

prepared Pt NPs supported on high surface area γ-Al$_2$O$_3$. Emphasis is given here to monitoring the changes in the structure of the NPs under *in situ* conditions (*e.g.* before, during and after ligand removal and under diverse chemical environments) *via* EXAFS. Our *in situ* real-time measurements were carried out in the presence of O$_2$, H$_2$O, or H$_2$ up to 450 °C and in H$_2$ up to 800 °C. Our spectroscopic results are compared with *ex situ* TEM data acquired after three different NP pretreatments (as prepared samples) and after high temperature annealing. The temperature regimes selected in this study are relevant to industrial catalytic processes. For example, operating temperatures of about 450 °C have been reported for *n*-heptane reforming,[52] NO oxidation,[53] and steam reforming of dimethyl ether,[54] while steam methane reforming[55] and sulfuric acid decomposition processes[49] were found to take place in the 800 °C temperature regime.

2. Experimental details

(a) Sample preparation

Inverse micelles were created by dissolving polystyrene 2-vinylpiridine [PS(27700)-P2VP(4300) for S1–S2 and PS(16000)-P2VP(3500) for S3–S5] in toluene. Subsequently, the micellar cages were loaded with Pt (H$_2$PtCl$_6$ precursor) with a 0.1 metal-to-polymer head (P2VP) ratio for S1–S2 and 0.05 ratio for S3–S5. The NP solution was then mixed with nanocrystalline γ-Al$_2$O$_3$ (surface area > 150 m^2 g^{-1}) at a loading of 1 wt% Pt, and allowed to dry in air at 60 °C. Additional details on the sample preparation can be found in ref. 16, 20 and 56–60.

Following this synthesis, the final size of the encapsulated NPs is determined by the length of the polymer head (P2VP) and by the metal/P2VP ratio. For this study, we have prepared five separate samples with identical synthesis parameters (same NP solutions) for S1–S2 (first sample set) and S3–S5 (second sample set), and exposed them to three different pre-treatments and annealing environments in order to explore their influence on the dispersion and thermal stability of the NPs. Sample 1 (S1) was annealed in 70% O$_2$ (balanced by He) at 200 °C for 1 hour (as-prepared state). Sample 2 (S2) was only dried in air at 60 °C (as-prepared state). Subsequently, both samples were transferred into a high-temperature reactor cell compatible with EXAFS measurements and exposed to the following *in situ* treatments: (i) S1 was annealed in 100% O$_2$ between 375 °C and 400 °C for ~4.5 hours; (ii) S2 was annealed in 50% H$_2$ (balanced by He) at 400 °C for ~1.1 h. After the former distinct pre-treatments, both samples were isochronally step-wise annealed in H$_2$ (50% H$_2$ balanced with He with a total flow of 50 ml min^{-1}) from 400 °C to 800 °C for a total of ~6 hours (~1.0 h at 400 °C, ~1.4 h at 500 °C, ~1.2 h at 650 °C, ~2.3 h at 800 °C). It should be noted that after the latter

treatment at 800 °C, the X-ray photoelectron spectroscopy (XPS) data from these samples revealed the complete absence of residual ligands (no C-1s signal), Fig. S1 (ESI†). As described in detail in ref. 58, the annealing of similar inverse micelle prepared Pt NPs up to 500 °C in H$_2$, did not lead to the complete removal of the encapsulating polymeric ligands, while an absence of carbon is observed on the same sample when annealed at/above 375 °C in O$_2$.[20,58,60] Therefore, the starting state of NPs in S1 before the H$_2$ annealing at/above 400 °C is characterized by ligand-free NPs, while residual polymeric ligands are still expected on S2 NPs at the same stage.

Samples 3–5 were prepared with a slightly different NP solution with respect to samples S1 and S2, as described above, also leading to the formation of small NPs. These three identical samples were pre-treated in O$_2$ (70%) at 375 °C for 24 h and subsequently *in situ* reduced in H$_2$ (50%) at 375 °C for 30 min. Next, sample S3 was annealed in O$_2$ at 450 °C for 3 hours and sample S4 was dosed with water at atmospheric pressure using a bubbler and annealed in the presence of water vapor and He at 450 °C for 3 hours. Finally, sample S5 was annealed in H$_2$ at 450 °C for 3 h. At the end of each thermal treatment, all three samples were reduced in hydrogen at 375 °C and the final NP size evaluated *in situ via* EXAFS (in H$_2$) and *ex situ via* STEM, both at RT. The summary of different treatment for each sample is provided in Table 1.

(b) Sample characterization

High-Angle Annular Dark Field (HAADF) STEM measurements were performed on our samples before and after the coarsening investigation to obtain information on the NP size. A suspension created by mixing the powder samples with ethanol was placed on a carbon-coated TEM Cu grid. HAADF images of the Pt/γ-Al$_2$O$_3$ samples were acquired under scanning mode within a JEOL 2010F TEM operated at 200 kV. The probe size of the STEM is about 0.14 nm.

The high absorption of the nanocrystalline alumina support makes measurements of very small Pt NPs (<1 nm) difficult, even in the HAADF STEM mode, due to the poor contrast. In addition, such images only provide information on the NP diameter, but not on the NP shape or structure. Nevertheless, bright field TEM investigations of these types of samples are also not possible due to the high internal structural disorder of the small NPs, especially when studied *ex situ* after air exposure, *i.e.*, in the presence of PtO$_x$ species.

TEM images of the as-prepared, 800 °C H$_2$-annealed, and 450 °C H$_2$O, O$_2$, and H$_2$-annealed samples were acquired, Fig. 1 and 3. NP diameter histograms obtained by measuring the full width at half-maximum of at least 600 particles per histogram are shown in Fig. 2 and 4. The size histograms presented here are limited by the resolution of the TEM and

Table 1 Summary of the *ex situ* and *in situ* treatments applied to samples S1–S5

Sample Pt NPs/γ-Al$_2$O$_3$	Ex situ pre-treatment	In situ pre-treatment	In situ thermal treatment
S1	200 °C (1 h in O$_2$)	375–400 °C (1.1 h in O$_2$)	400–800 °C (6 h in H$_2$)
S2	60 °C (3 h in air)	400 °C (1.1 h in H$_2$)	400–800 °C (6 h in H$_2$)
S3	375 °C (24 h in O$_2$)	375 °C (0.5 h in H$_2$)	450 °C (3 h in O$_2$)
S4	375 °C (24 h in O$_2$)	375 °C (0.5 h in H$_2$)	450 °C (3 h in H$_2$O)
S5	375 °C (24 h in O$_2$)	375 °C (0.5 h in H$_2$)	450 °C (3 h in H$_2$)

therefore, do not contain values below 0.14 nm. The error bars provided for the average TEM diameters are the standard deviation of the measured NP diameters. In the case of NPs which were not round in shape, for example, those that had sintered (S2), two diameters were measured (along the long and short axes) and averaged.

EXAFS measurements at the Pt-L$_3$ edge were conducted *in situ* during the different thermal treatments at the National Synchrotron Light Source (NSLS) at Brookhaven National Laboratory (BNL). The experiments were carried out in transmission (S1, S2) and fluorescence (S3–S5) modes at beamline X19A with the powder samples pressed into thin pellets and placed either inside a quartz tube surrounded by a clam shell furnace (S1, S2) or inside a reactor cell with heating and cooling capabilities (S3–S5). The quartz reactor tube is sealed by Kapton windows which are placed outside the furnace. The furnace was positioned on a motorized stage and the quartz tube axis was aligned along the X-ray beam direction. EXAFS spectra were measured at different temperatures from room temperature (RT) to 800 °C in 50% H$_2$ balanced by He. Up to a measurement temperature of 650 °C, several successive scans were similar, within the noise, and were averaged to improve the signal-to-noise ratio. At 800 °C, time-dependent changes in the NP structure (size) were observed for sample S1, and individual scans were used in the analysis. Samples S3–S5 were reduced *in situ* at 375 °C in H$_2$ and subsequently annealed in different environments (O$_2$, H$_2$O, and H$_2$) up to 450 °C for 3 hours.

The Athena and Artemis programs from the Ifeffit software package were used to process and analyze the EXAFS data acquired.[61,62] A Pt foil measured in reference mode was used to align different scans of the NP samples. The Artemis program[61–63] was used to fit the 1st nearest neighbor (NN1) Pt–Pt component of the EXAFS data. Theoretical EXAFS signals were constructed with the FEFF6 program[64] using the model structure of face centered cubic (fcc) Pt. The crystalline structure of all reduced Pt NPs investigated here is consistent with the fcc structure. Multiple scattering analysis (up to the 4th shell) of similarly prepared Pt NPs in our previous study also led to this conclusion.[60] Fig. S7 (ESI†) shows that all of the main fcc features in the EXAFS spectrum of the Pt foil (r-space representation up to 5 Å), are also present in our small NPs when measured in hydrogen after reduction. However, it should be noted that a hydrogen environment has been previously reported to result in NP faceting and improved crystalline ordering.[65] No clear evidence of the melting of the NPs under our experimental conditions was observed *via* EXAFS. For instance, the main fcc signatures in the EXAFS spectrum of a reference foil were also observed for S1 up to 800 °C when annealed in a hydrogen environment. Such features should have disappeared to a large extent upon NP melting.[66] Also, a sudden change in bond length (R) and bond length disorder (σ^2) is expected at the onset of melting,[66] which was not observed during our thermal treatments. However, we cannot rule out the melting of the smallest NPs in our samples (*e.g.* those in S1 at 800 °C) exclusively based on our *in situ* EXAFS data. The melting temperature of carbon supported Pt NPs with a size of 2.5 nm is calculated to be between 827 °C and 927 °C, while it could be as low as 427 °C–527 °C for

1.2 nm NPs.[67] Additionally, supports with high melting temperature, such as γ-Al$_2$O$_3$, used in this study have been shown to increase the melting temperature of the NPs.[68]

During the analysis of the time-dependent scans of S1, the bond length disorder parameters (σ^2), also known as EXAFS Debye–Waller factors (the mean square displacement of the scattering atom relative to the adsorbing atom), were constrained to be the same for all scans acquired at different times at each of the evaluated temperatures. This approximation is justified only at elevated temperatures, *i.e.*, when the size-dependent changes in the bond length disorder are small compared to the dynamic disorder.[69] Since the onset of particle coarsening for S1 was observed above 650 °C, when the dynamic contribution to σ^2 dominates, the former approach is justified. The 1st NN coordination numbers (CNs), Pt–Pt distances, and third cumulants were varied in the fits. Details on the quality of the fits of the EXAFS data of S1 and relevant fit parameters, including the k-ranges for the Fourier transform, are shown in Table S1 (ESI†) and for samples S3 and S4 in Table S2 (ESI†). In this manuscript, we only show a detailed analysis of the EXAFS data from sample S1 after annealing at high temperature, since significant coarsening was already observed in the differently pre-treated, as-prepared sample S2 at 400 °C. In addition, for the lower temperature thermal treatments (450 °C), the influence of the annealing environment on NP coarsening is also illustrated by comparing reduced samples measured in H$_2$ at RT before and after a given annealing treatment in O$_2$, H$_2$O, or H$_2$ (S3–S5).

3. Results and discussion

Fig. 1 presents high resolution HAADF STEM images of samples (a) S1 and (b) S2 as-prepared, and after annealing in H$_2$ up to 800 °C (c, d), respectively. The corresponding NP diameter histograms are shown in Fig. 2. Despite slightly different treatments (S1 was annealed in O$_2$ at 200 °C while S2 was annealed in air at 60 °C), the size distributions of the as-prepared clusters were found to be similar (0.3 ± 0.1 nm for both S1 and S2), as expected for samples synthesized using the same NP micelle solution. Since both samples show average diameters close to the microscope resolution, the actual particles might even be smaller in size. In both cases, the low annealing temperature used did not lead to the removal of the encapsulating ligands (PS-P2VP) (see XPS data of S2 as-prepared in Fig. S1, ESI†), and we do not expect these organic ligands to be detected *via* HAADF-TEM.

In order to gain further insight into the evolution of the structure of our NPs, *in situ* EXAFS measurements were carried out. It should be highlighted that EXAFS is a complementary method to TEM, also presenting certain valuable advantages: (i) it can be used to extract information on the evolution of the NP size (*via* the atomic coordination numbers) during a given thermal or chemical treatment. In the present study, thermal treatments up to 800 °C in H$_2$ and up to 450 °C in H$_2$, O$_2$ and H$_2$O were implemented. Such *in situ* investigation of the evolution of the NP size at elevated temperatures and in the presence of gases is at present not possible in environmental TEMs for NPs of this small size (∼1 nm). (ii) EXAFS can provide insight not only into the NP size at a
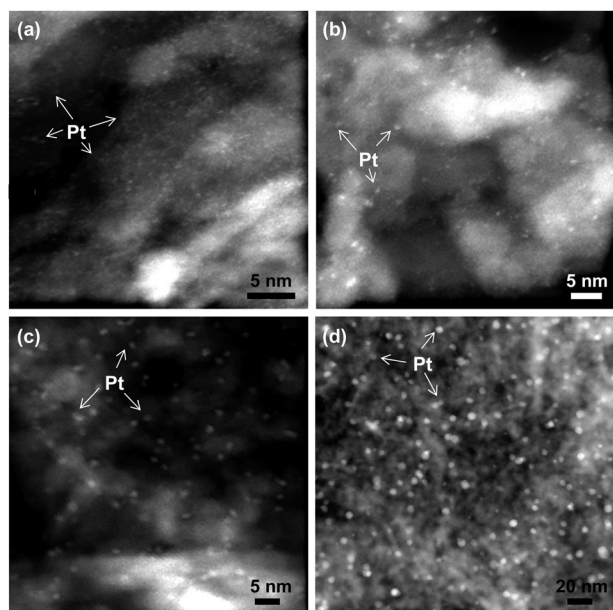
Fig. 1 Representative HAADF STEM images of samples (a, c) S1 and (b, d) S2 containing inverse micelle prepared Pt NPs supported on γ-Al_2O_3. Both samples were prepared with an identical inverse micelle prepared NP solution, but, different pre-treatment conditions were used. Sample S1 was annealed in O_2 at 200 °C for 1 hour after drying (a), while sample S2 was only dried in air at 60 °C (b). After the distinct pre-treatments, S1 was first annealed in O_2 at 400 °C followed by a stepwise annealing in H_2 from 400 °C to 800 °C (c). Sample S2 was never exposed to O_2, only stepwise annealed in H_2 from RT to 800 °C (d).
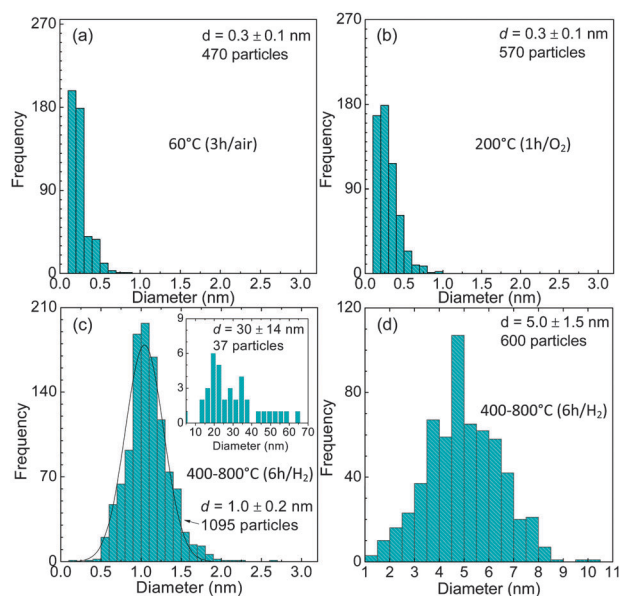

Fig. 2 Histograms of nanoparticle diameters extracted from HAADF STEM images of samples (a, c) S1 and (b, d) S2 shown in Fig. 1. The data in (a) and (b) correspond to the as-prepared samples, while (c) and (d) were obtained after stepwise sample annealing in H_2 up to 800 °C. The inset in (c) shows a small fraction of large NPs observed on S1 after annealing.

given temperature and under a given chemical environment, but also into the structure of the NPs[60,70] (*e.g.* fcc or icosahedral). For NPs within this size range ($\sim$1 nm), this is not possible
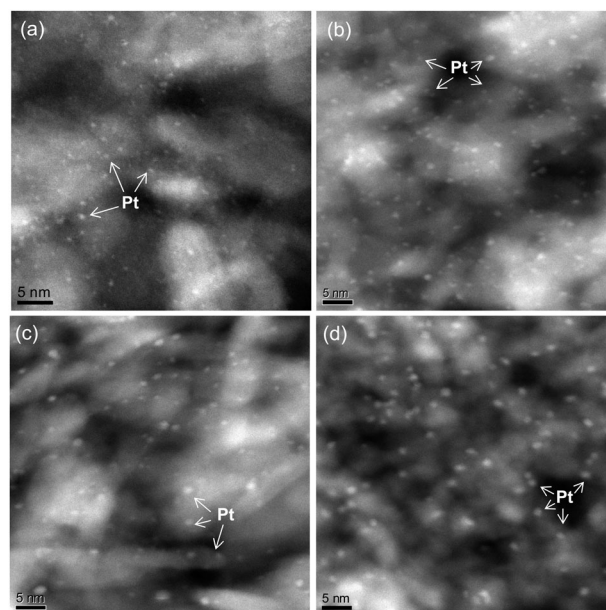
Fig. 3 Representative HAADF STEM images of samples containing inverse micelle prepared Pt NPs supported on γ-Al_2O_3: (a) S3–S5 as prepared, (b) S3 after annealing in O_2 at 450 °C, (c) S4 after annealing in He + H_2O at 450 °C, and (d) S5 after annealing in H_2 at 450 °C. All samples were prepared with an identical inverse micelle prepared NP solution.
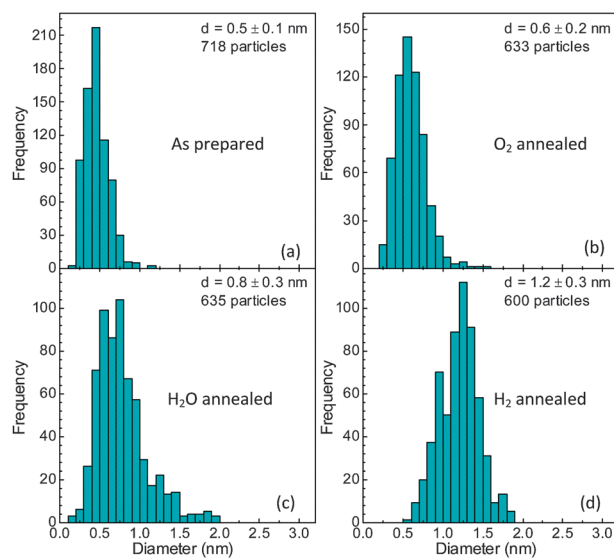

Fig. 4 Histograms of NP diameters extracted from HAADF STEM images of samples (a) S3–S5 as prepared, (b) S3 after annealing in O_2, (c) S4 after annealing in He + H_2O, and (d) S5 after annealing in H_2 shown in Fig. 3.

via ex situ TEM, since the NPs can only be resolved in HAADF dark field mode, where only the NP diameter, and if calibrated, the number of atoms can be obtained, but not the lattice parameter or structure. In addition, the EXAFS measurements can be done after NP reduction (in H_2), and H_2 is known to induce faceting and improve the internal ordering of the NPs. The *ex situ* TEM work must be done on "air exposed" samples, which will intrinsically have a worse ordering, or no long-range ordering at all, due to the formation of

PtO$_x$ species on the NP surface. (iii) EXAFS can provide information on Pt–Pt distances for very small NPs,[71,72] whose structure cannot be resolved *via* ex-situ TEM. Even *in situ* bright field TEM measurements on reduced NPs (*e.g.* in H$_2$) are extremely challenging for NPs within this size range, and have not been reported for the system at hand (Pt NPs on nanocrystalline γ-Al$_2$O$_3$). (iv) EXAFS can also provide information on the degree of internal disorder of the NPs *via* the "static disorder" parameter.[71] (v) EXAFS can provide insight into the presence of adsorbates on the NP surface as well as on the formation of oxidic species.[19,20,73] Such information would not be detected *via* ex situ TEM for very small NPs, especially if such oxide shells are highly disordered (amorphous). (vi) EXAFS provides ensemble averaged values from the entire sample while TEM provides local information.

As was described in the experimental section, the as-prepared samples were subsequently subjected to two different treatments before high temperature annealing. Sample S1 was annealed in O$_2$ up to 400 °C and S2 in H$_2$ up to 400 °C. After such *in situ* treatments, identical EXAFS measurements carried out at 400 °C in H$_2$ revealed significantly larger CNs for the NPs pre-treated in H$_2$, namely, 9.3 ± 1.6 for S2 *versus* 6.9 ± 0.7 for sample S1. Subsequent stepwise isochronal annealing of both samples in H$_2$ from 400 °C to 800 °C led to a clearly distinct coarsening behavior, as evidenced by the TEM images in Fig. 1(c) for S1, (d) for S2, and the corresponding histograms in Fig. 2(c) and (d). From the analysis of nearly 1100 NPs, the average NP diameter in S1 after annealing at 800 °C in H$_2$ was found to be 1.0 ± 0.2 nm. Nevertheless, a few NPs > 10 nm (37 NPs) were also observed, Fig. 2(c) (inset). On the other hand, significant overall coarsening was observed for S2 after an identical high temperature treatment, with an average final NP diameter of 5.0 ± 1.5 nm. Since for large NPs (> 3 nm) bulk-like EXAFS 1st NN CNs are obtained (12 for bulk Pt), and the NPs in S2 were already large according to EXAFS after the pre-treatment in H$_2$ (400 °C), EXAFS data acquired for this sample above 400 °C are not shown in this report.

Fig. 3 displays HAADF-STEM images of samples S3–S5 after different thermal treatments: (a) as-prepared (all three identical samples annealed in O$_2$ at 375 °C for 24 h), (b) S3 after annealing in O$_2$ + He at 450 °C (3 h), (c) S4 after annealing in H$_2$O + He at 450 °C (3 h), and (d) S5 after annealing in H$_2$ + He at 450 °C (3 h). All three samples were reduced in H$_2$ at 375 °C (30 min) after the former treatments before the subsequent room temperature-EXAFS and STEM analyses. The corresponding TEM NP diameter histograms are shown in Fig. 4. Additional lower magnification STEM images of S3–S5 demonstrating the overall homogeneity of the NP size and substrate dispersion are shown in Fig. S2 (ESI†). The ligand-free as-prepared samples were characterized by an average NP size distribution of 0.5 ± 0.1 nm. Water dosing and subsequent annealing at 450 °C in H$_2$O + He did not lead to drastic changes in overall sample morphology, although some sintering was observed: 0.8 ± 0.3 nm (S4). On the other hand, a drastic increase in the average NP size was observed when the same sample (a different portion of the same identical starting sample) was annealed in hydrogen, 1.2 ± 0.3 nm (S5), suggesting enhanced atomic/NP mobility in the

reducing environment. Surprisingly, when the same sample was annealed in O$_2$, lack of sintering was observed: 0.6 ± 0.2 nm (S3). These results are in agreement with the observations made for S1 and S2, where pre-treatments in O$_2$ at 400 °C contributed to the stabilization of the NPs. Since STEM is a local probe allowing sampling of relatively small sample regions, our observations will be compared to ensemble-averaging data extracted from EXAFS measurements.

Fig. 5 shows Fourier transforms of EXAFS spectra of S1 acquired *in situ* at various temperatures and under different gaseous environments. Representative EXAFS data in *k*-space from S1 are shown in Fig. S3 (ESI†). From 400 °C to 650 °C, multiple, nearly identical EXAFS scans (3–6 scans) acquired at the same temperature were merged. Systematic differences were observed among individual scans acquired at 800 °C, and therefore, those data were not merged. Three representative scans acquired at 800 °C are shown in Fig. 5. The spectrum corresponding to the as-prepared state of S1 is characterized by a large peak near 1.7 Å (phase shift uncorrected). This feature corresponds to a convolution of Pt–O and other bonds related to the presence of the polymer[60] and residual species from the metal precursor salt around the Pt ions (*e.g.* Pt–N, Pt–C, Pt–Cl from PS-P2VP and H$_2$PtCl$_6$). Annealing in O$_2$ at 375 °C leads to the removal of the polymer, and the low-r component observed in the spectrum, now at ∼1.6 Å, can be entirely assigned to Pt–O bonds in PtO$_x$ species (corresponding to a real space Pt–O distance of ∼2 Å).[20] *In situ* annealing at 400 °C in H$_2$ leads to the disappearance of the former feature and complete reduction of the Pt NPs. After NP reduction, Fig. 5 reveals a decrease in the overall intensity of the Pt–Pt EXAFS signal with increasing measurement temperature up to 650 °C, which is consistent with the effect of thermal bond length disorder. Interestingly, a sudden increase in the magnitude of the Fourier transform main Pt–Pt component is observed at 800 °C (see inset in Fig. 5). This effect can only be explained if the growth (coarsening) of the NPs is considered, since the increase in the 1st NN CN will
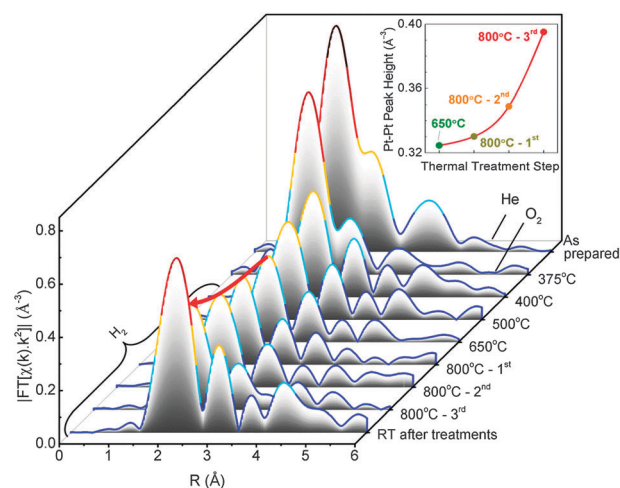

Fig. 5 Fourier transform magnitudes of k^2-weighted Pt L$_3$-edge EXAFS spectra of S1 acquired *in situ* at various stages of a thermal treatment. The spectra are organized chronologically, from top to bottom. The inset displays the peak height of the main Pt–Pt component extracted from the EXAFS data in the main panel at/above 650 °C.

compensate the decrease in the signal induced by thermal disorder. At the same time, the disorder is expected to decrease due to the larger fraction of interior, bulk-like bonds within the larger NPs. That effect also leads to an increase in the FT magnitude of the Pt–Pt peak. We do not report the disorder values for S1 at the different temperatures since the trend was not distinguishable outside experimental uncertainties. From the fit of the EXAFS spectra in Fig. 5, the Pt–Pt distances and 1st NN CNs were obtained at different temperatures. A representative spectrum acquired in H$_2$ at 500 °C and fit are shown in Fig. 6(a). For S1 in H$_2$, the Pt–Pt distances start at 2.73(3) Å (400 °C) and increase with increasing annealing temperature to 2.76(3) Å (650 °C), until reaching a maximum of ∼2.80(3) Å at 800 °C, and then decreased to 2.75(2) Å at RT after NP coarsening, Fig. S4 (ESI†). The changes in the Pt–Pt distances measured can be assigned to several concomitant factors: (i) the increase in the NP size with increasing annealing temperature, since small NPs are normally characterized by a contraction of the interatomic distances. Nevertheless, the temperature-dependent hydrogen coverage on the NP surface must also be considered, since H adsorption has been shown to lead to an increase in the Pt–Pt distances;[69,74,75] (ii) positive thermal expansion. According to our nearly constant EXAFS CNs, the increase in the Pt–Pt distances at and

below 650 °C should not be explained in terms of NP growth (coarsening), but should rather be assigned to the conventional positive thermal expansion. The presence of hydrogen on the NP surface cannot be used to explain the increase in the distances with increasing annealing temperature, since it is expected to desorb below our minimum annealing temperature of 400 °C. At the high measurement temperatures employed here, the H$_2$ coverage effect should not strongly impact the bond lengths.

Fig. 6(b) illustrates the *in situ* time evolution of the 1st nearest neighbor CNs obtained in hydrogen for S1 at different annealing temperatures. The 1st NN CNs remain stable up to 650 °C (∼6.9), but were found to increase rapidly after reaching 800 °C (∼8.9 for the last scan at this temperature). The latter is assigned to the onset of coarsening at 800 °C. After cooling S1 to RT, the 1st NN coordination number remains stable (∼9.2). The relatively low maximum CN observed for S1 after the high temperature annealing process indicates the enhanced thermal stability of these NPs as compared to S2, which was characterized by a CN of ∼12 at RT after annealing in H$_2$ at 800 °C (not shown). The latter trend shows that the pretreatment in O$_2$ applied to S1 served to stabilize the NPs and minimize their coarsening. From the *in situ* EXAFS 1st NN CNs of S1, the thermal evolution of NP size can be extracted *via* Fig. 7, as it is shown in Fig. 6(c). Fig. 7 displays the correlation between the 1st NN CNs and the NP diameter obtained from a database of three-dimensional fcc NP shapes. Since the coordination numbers of atoms in a NP are related to their size and shape, it is in principle possible to estimate the size of NPs *via* EXAFS if the shape is known.[76,77] However, shape analysis using EXAFS data is challenging, since it requires information not just on the 1st NN CN (reported here for the EXAFS data acquired at different temperatures), but also on the 2NN–4NN CNs.[70,71,76,77] The detailed information needed for shape analysis must be extracted from multiple-scattering (MS) analysis of EXAFS data,[70] which cannot be implemented with the relatively low *k*-range of the EXAFS spectra obtained at high temperatures
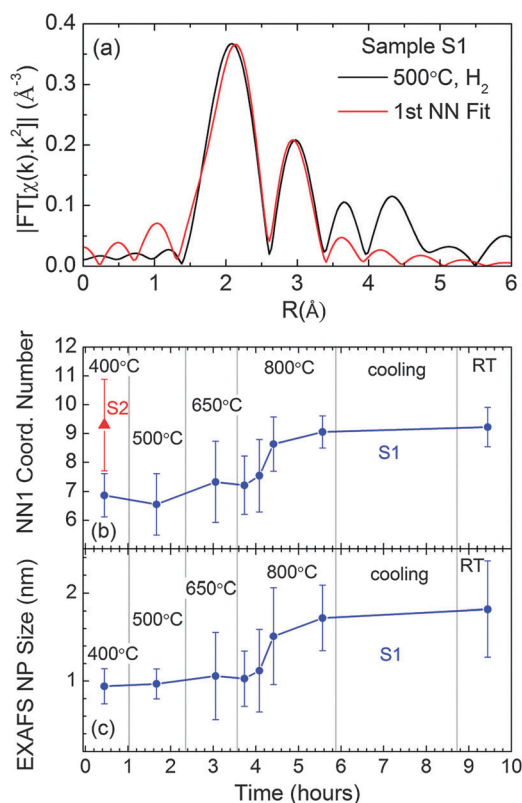

Fig. 6 (a) Fourier transform magnitudes of a k^2-weighted Pt L$_3$-edge EXAFS spectrum acquired for S1 at 500 °C in H$_2$, along with the corresponding first shell fit using only a metallic Pt–Pt component. Time evolution of (b) the first-nearest-neighbor (NN1) coordination number of S1 and (c) the NP size extracted from EXAFS data. In (b), the NN1 coordination number of S2 at 400 °C (triangle) is shown for comparison purposes.
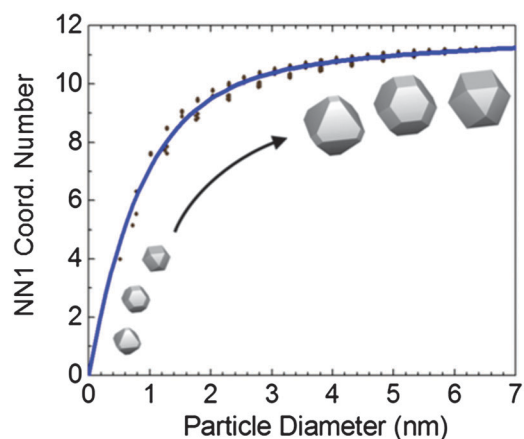

Fig. 7 Evolution of the NN1 coordination numbers of several fcc NP shapes displayed *versus* the NP diameter. Some of the model NP shapes used to generate this plot are shown for reference as insets. The curve fitted to the data points serves as a guide for obtaining NP diameter estimates based on EXAFS NN1 CNs.

11462 | *Phys. Chem. Chem. Phys.*, 2012, **14**, 11457–11467

This journal is © the Owner Societies 2012

due to the disorder-induced signal damping. The 3D NP shapes shown as the inset in Fig. 7 represent some of the possible fcc NP shapes which might be obtained for a given NP size. We have selected those 3D NP shapes that were previously observed to better match analogously prepared Pt NPs.[60] Furthermore, 3D NP shapes were obtained from the multiple scattering analysis of the RT data of S1 after annealing at 800 °C (see details in the ESI† and Table S3). It should be also noted that determining the NP size *via* EXAFS for large NPs (> 2 nm) is challenging, since as can be seen in Fig. 7, a larger fraction of NP sizes would result in similar coordination numbers (within experimental error bars). For this reason, we have not used this method to estimate the size of the large NPs in S2, but only those in S1 (∼ 1 nm on average according to TEM after coarsening), and have limited our description of the coarsening behavior of S2 to our TEM observations. This also explains the larger error bars obtained for the EXAFS NP sizes of S1 at 800 °C, when NP coarsening was found to set in.

Fig. 6(c) reveals an average EXAFS NP size after coarsening of 1.8 ± 0.5 nm, while the majority of the TEM NPs observed after annealing at 800 °C had an average diameter of ∼ 1.0 nm, although a reduced number (∼ 3%) of large NPs (> 10 nm) were also observed *via* TEM. In order to understand the difference between the EXAFS and TEM NP sizes, the intrinsic distinctions existent between both techniques must be noted. In particular, EXAFS is a volume-averaging technique providing information from the entire sample, while TEM is a local technique. Therefore, the best comparison between EXAFS and TEM data is done by using volume-averaged TEM sizes. In our case, for the majority of NPs in S1, the volume-averaged TEM diameter (after heating at 800 °C) is 1.3 ± 0.3 nm, which is in better agreement with the EXAFS size. Furthermore, since small NPs are harder to detect *via* TEM, caution must be taken in order not to overemphasize the relative number (particle density) of large NPs present in a given sample, since those are the only ones which will be detected in low magnification images. This is especially important when comparing TEM to EXAFS NP sizes, since due to the mentioned volume-averaging in EXAFS, large NPs hold a strong weight in EXAFS results.

In addition to the investigation of NP coarsening for two samples identically synthesized but exposed to two different pre-treatments and subsequently annealed in hydrogen, the role of the gaseous environment during annealing was also studied using as a target system three identical samples containing ligand-free reduced inverse micelle prepared Pt NPs (S3–S5). Fig. 8 displays r-space Fourier-transform EXAFS data of those samples measured at room temperature in H_2 after reduction at 375 °C in H_2 (30 min) before (labeled as-prepared) and after *in situ* thermal treatments at 450 °C in O_2, H_2O vapor, and H_2, in each case for 3 hours. Representative EXAFS data in k-space of S3–S5 measured at room temperature in H_2 after annealing (450 °C) under different environments, together with similar data from the as-prepared sample (after reduction in H_2 at 375 °C) are shown in Fig. S5 (ESI†).

After the former treatments, all samples were reduced in H_2 at 375 °C before the acquisition of the final RT-EXAFS data in H_2 shown in Fig. 8. A representative 1st-shell fit is shown
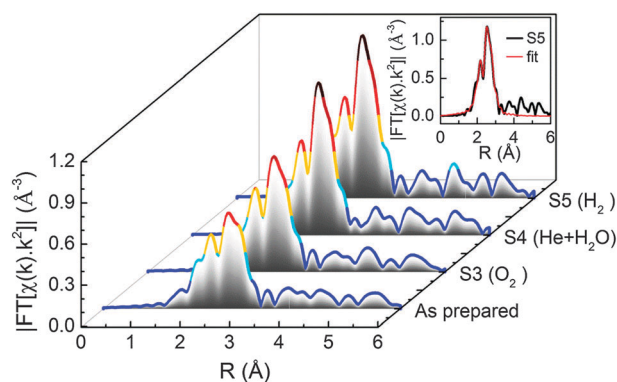

Fig. 8 Fourier transform magnitudes of k^2-weighted Pt L_3-edge EXAFS spectra acquired for samples S3–S5 at RT in H_2 after an initial common pre-treatment in O_2 at 375 °C followed by reduction at 375 °C in H_2 and subsequent annealing in O_2 (S3), H_2O (S4) and H_2 (S5) at 450 °C for 3 hours. All samples were reduced *in situ* at 375 °C in H_2 before the acquisition of the EXAFS data. A representative first-shell fit of the EXAFS data of S5 is included as the inset.

as inset, and the results from those fits, including 1st nearest neighbor CNs, Pt–Pt distances and disorder (σ^2) are included in Table 2. After reduction in H_2 at 375 °C, the as-prepared samples were characterized by NN1 = 6.5 ± 0.4. Annealing in oxygen for several hours at 450 °C did not induce any clear changes in the average NN1, with NN1 = 6.9 ± 0.4 (S3), indicating the stability of the NPs in the oxidizing environment. When the same sample (a different portion of the same sample) was pre-dosed with water and annealed in a water-containing environment (in He), a small change in the overall NP size was observed *via* EXAFS, with NN1 = 7.3 ± 0.3 (S4). In contrast, an identical thermal treatment in H_2 was found to lead to clear NP sintering, with NN1 = 8.3 ± 0.4 (S5). It should be noted that the EXAFS findings are in good agreement with our local TEM observations (Fig. 3 and 4). Furthermore, following Fig. 7, NP sizes can also be estimated based on the EXAFS NN1 coordination numbers. Such data are included in Table 2, and compared to volume-weighted STEM diameters. An overall good agreement between the EXAFS and STEM NP sizes is observed. Moreover, as can be seen in Table 2, due to the overall small final average size of the NPs in our samples (< 1.2 nm according to TEM), the Pt–Pt distances obtained are smaller than those of bulk Pt, a contraction which is expected for small NPs. Further, the latter effect is observed even though all samples were measured in H_2, which has been shown to relax the Pt–Pt bonds.[57,69,72,79] Additionally, a correlation between the final NP size and the magnitude of the EXAFS disorder was obtained, with the largest values obtained for the as-prepared and O_2-annealed samples (0.0073–0.0078 Å^2), and the smallest values for the H_2O and H_2 annealed samples (0.0066–0.0068 Å^2). For comparison, a value of 0.005 Å^2 was obtained from the fit of a bulk Pt foil.

Summarizing, our study revealed a clearly distinct coarsening behavior of two identically prepared samples (S1, S2) exposed to two distinct pre-treatments before high temperature annealing and of three identical samples after annealing in different environments (S3 in O_2, S4 in H_2O, S5 in H_2). This is schematically depicted in Fig. 10. As was described above,

Table 2 First-nearest neighbor coordination number (NN1), Pt–Pt distance (R), disorder (σ^2), and NP size extracted from EXAFS and STEM data (diameter) after sample exposure to different *in situ* thermal treatments in O_2 (S3), H_2O (S4), and H_2 (S5)

Sample Pt NPs/γ-Al$_2$O$_3$	NN1	R (Å)	σ^2 (Å^2)	TEM NP diameter (nm)	TEM volume-weighted NP diameter (nm)	EXAFS NP size (nm)
S1–S2 as prepared	—	—	—	0.3(1)	—	—
S1 in H$_2$ at RT, after annealing in H$_2$ at 800 °C	9.2(7)	2.75(2)	0.0076(8)	1.0(2)	1.3(3)	1.8(5)
S2 in H$_2$ at RT, after annealing in H$_2$ at 800 °C	12.3(9)	2.75(2)	0.0068(10)	5.0(15)	—	—
S3–S5 in H$_2$ at RT, after reduction in H$_2$ at 375 °C	6.5(4)	2.749(4)	0.0078(4)	0.5(2)	0.6(2)	0.9(1)
S3 in H$_2$ at RT, after annealing at 450 °C in O$_2$ + He	6.9(4)	2.750(3)	0.0073(3)	0.6(2)	0.8(3)	1.0(1)
S4 in H$_2$ at RT, after annealing at 450 °C in H$_2$O + He	7.3(3)	2.752(2)	0.0066(2)	0.8(2)	1.2(4)	1.1(1)
S5 in H$_2$ at RT, after annealing at 450 °C in H$_2$ + He	8.3(4)	2.743(2)	0.0068(2)	1.2(3)	1.4(3)	1.4(2)
Pt foil	12	2.763(1)	0.0050(1)			

enhanced thermal stability (no coarsening up to 650 °C) was observed for the sample pre-treated in O$_2$ at 400 °C, S1. This result is in agreement with previous findings by Alexeev *et al.*[41] demonstrating lack of sintering for Al$_2$O$_3$-supported Pt NPs prepared *via* precipitation/impregnation upon annealing in O$_2$ at 400 °C. Au NPs supported on SiO$_2$ were also found to be thermally stable up to 500 °C when annealed in O$_2$-containing environments.[25] On the other hand, the presence of much larger NPs was inferred from the EXAFS CNs of the sample pre-treated only in H$_2$ at 400 °C (S2), Fig. 6(b). Furthermore, even after the onset of coarsening observed for S1 at 800 °C *via* EXAFS, the majority of the NPs in this sample remained small according to the relatively low final CNs (~9.2). This was corroborated by our *ex situ* STEM images showing ~1 nm NPs for S1 after coarsening, while ~5 nm were detected in S2. The mechanism underlying the enhanced thermal stability of O$_2$-pre-treated samples (S1 here) is still not well understood. However, it is likely related to the concomitant formation of PtO$_x$ species, as it is shown in our EXAFS data of Fig. 8 and 9, where NPs annealed in O$_2$ were found to be more thermally stable (S3) than those heated in H$_2$ (S5). The presence of such species might contribute to strengthening the binding between the Pt NPs and the Al$_2$O$_3$ support, as suggested for O$_2$-annealed Au NPs on SiO$_2$[25] and Pd on Al$_2$O$_3$.[15] Interestingly, Goeke and Datye[26] previously reported smaller NP sizes for Pd NPs synthesized by electron beam evaporation when annealed in O$_2$ at 700 °C as compared to identical samples pre-annealed in an inert atmosphere. This effect was also assigned to the formation of PdO$_x$ species. The same explanation is valid when the distinct stability of samples S3 (annealed in O$_2$) and S5 (annealed in H$_2$) is considered, with reducing annealing environments favoring the sintering of the inverse micelle prepared NPs above 375 °C, Fig. 10.

Even though the present EXAFS and TEM data cannot be used to determine the coarsening mechanism underlying our experimental observations,[80] some similarities exist between the behavior of the highly unstable Pt NPs in S2 encapsulated by PS-P2VP at/below 400 °C, and Au NPs in poly(methyl methacrylate) thin films.[27] For the latter system, two different stages were observed in the NP growth. An initial growth stage at low temperature and/or, for short annealing times, involving both Ostwald-ripening (OR, NPs grow *via* the transfer of atoms from small to large NPs) and diffusion–coalescence (DC, entire NPs diffuse on the support surface, collide, and fuse into larger clusters), followed by a second sintering stage once the organic ligands had been completely desorbed from
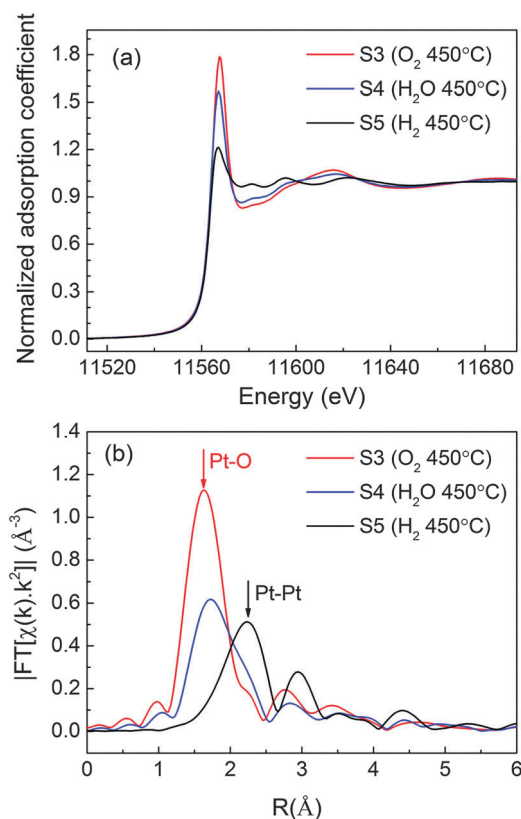
Fig. 9 (a) Normalized absorption coefficient corresponding to the Pt-L$_3$ edge and (b) Fourier transform magnitudes of k^2-weighted Pt L$_3$-edge EXAFS spectra of samples S3–S5 acquired at 450 °C in O$_2$, H$_2$O and H$_2$.

the NP surface; purely characterized by diffusion coalescence processes. In our example, ~400 °C is the critical temperature above which significant ligand removal occurs for the H$_2$-annealed NPs (although not complete up to at least 500 °C).[58] Following Meli and Green,[27] the coarsening observed for S2 below that temperature is likely due to combined OR/DC phenomena, with OR dominating for large initial interparticle distances; while the diffusion of whole clusters is likely to set in at high temperature once the stabilizing ligands have been removed.

The case of NPs in S1 is even more interesting, since in the complete absence of the protecting ligands (after annealing in O$_2$ at 375 °C), no sintering was detected at least up to 650 °C. The same applies to S3, which was annealed in O$_2$ at 450 °C for 3 hours. An initial O$_2$-mediated NP redispersion might
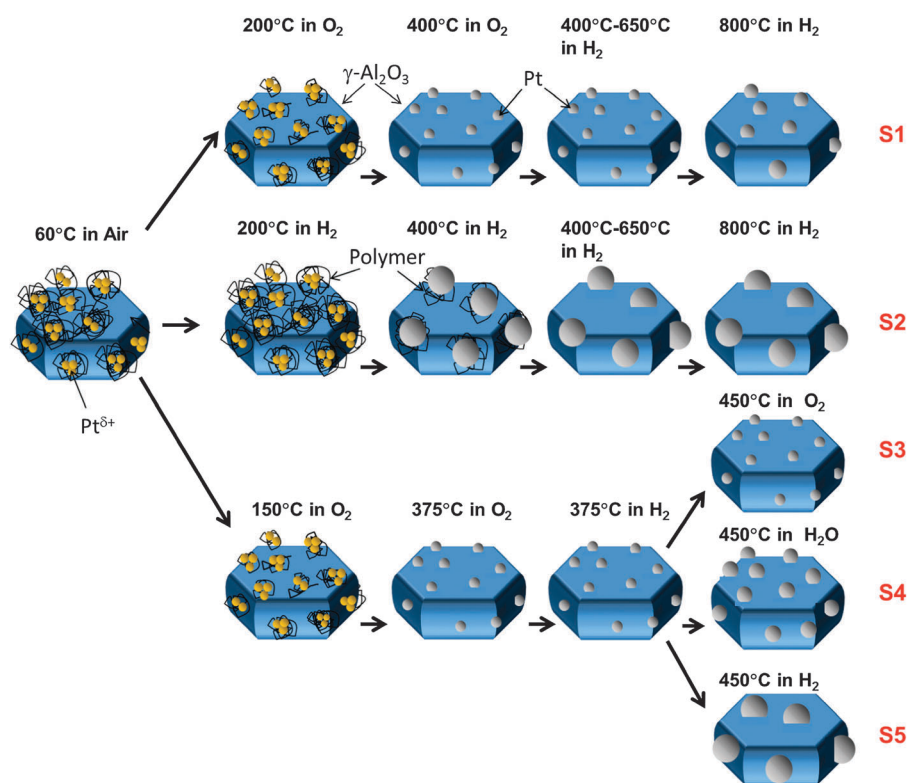
11464 | *Phys. Chem. Chem. Phys.*, 2012, **14**, 11457–11467

This journal is © the Owner Societies 2012

Fig. 10 Schematic representation of the evolution of the structure and chemical state of our inverse micelle prepared Pt/γ-Al$_2$O$_3$ samples (S1–S5) under various thermal and chemical treatments inferred from the analysis of *in situ* EXAFS and *ex situ* STEM data.

contribute to this effect, since coalescence phenomena have been shown to be less favorable when the NPs are widely spaced.[81] More importantly, the pre-treatment in O$_2$ is likely to affect the structure, chemical state, and density of defects in the Al$_2$O$_3$ surface, which are also expected to influence the stability of the NPs. In fact, the desorption of hydroxyl groups from Pt NP/γ-Al$_2$O$_3$ samples at/above 580 °C has been reported,[41] with $\sim$80% OH removal at 600 °C.[16] If OH species were to act as anchoring sites for the Pt NPs, as previously suggested for Pd/Al$_2$O$_3$[15] and Au/MgO,[78] the desorption of the latter would lead to sintering. Since significant loss of OH groups is expected at/above 650 °C, a plausible explanation for the onset of sintering in S1 is drastic morphological and chemical changes in the support surface. This effect adds to the additional partial de-stabilization of the Pt NPs expected to occur after reduction of the PtO$_x$ species by the H$_2$ treatment at 400 °C, since weaker NP/support bonding has been reported for metallic NPs on oxides, as for example reduced Pd on Al$_2$O$_3$.[15] Therefore, our results indicate that pre-treatments in O$_2$ might be valid alternatives to stabilize as well as to regenerate coarsened catalysts *via* catalysts redispersion, although the possible loss of Pt through the formation of volatile PtO$_x$ species must also be taken into account.[16] In our example, by comparing the edge jump (Pt-L$_3$) of S1 before and after annealing in O$_2$ at 400 °C, no loss of Pt was evidenced. However, such an effect cannot be excluded after annealing treatments in O$_2$ at higher temperatures.[16] Regarding the stabilizing effect of hydroxyl groups against NP sintering,[78,82] our EXAFS and TEM data of the sample pre-dosed with water and annealed in water vapor at

450 °C (S4) demonstrate that such pre-treatment contributes to the partial stabilization of the NPs (as compared to S5 annealed in H$_2$), although it is less efficient than the pre-treatment or annealing in an O$_2$ atmosphere (S3). Fig. S6 (ESI†) shows XANES data of S4 acquired during the thermal treatment at 450 °C in H$_2$O. The progressive increase in the intensity of the Pt-L$_3$ absorption peak (white line) with increasing annealing time demonstrates the gradual oxidation of the NPs, which might explain their partial stabilization, as was the case of the NPs in S3 after a similar treatment in oxygen.

Chlorine has been shown to play a crucial role in NP coarsening and redispersion.[83,84] Although the precursor metal salts used here contain Cl (H$_2$PtCl$_6$), high resolution XPS data revealed the absence of Cl from our samples after thermal pre-treatments at/above 350 °C.[13,60] Therefore, the possible contribution of Cl to the results shown here for samples S3–S5 is ruled out, since these samples were pre-annealed at 375 °C. For samples S1, S2, our sintering study started after sample annealing at 400 °C, which also ensured the removal of residual Cl.

While platinum oxide species are unstable at high temperature ($\sim$450 °C) under ultrahigh vacuum (UHV) or reducing atmospheres, they can be formed and stabilized at such temperatures in oxygen environments. Fig. 9 shows the XANES and EXAFS data obtained at 450 °C for samples S3, S4, and S5 under O$_2$, H$_2$O, and H$_2$ environments, respectively. From both, the increase in the white line intensity, Fig. 9(a), and appearance of a Pt–O contribution in the EXAFS spectra at $\sim$2 Å, Fig. 9(b), the formation of stable PtO$_x$ species on our samples is concluded. Although the increase in the XANES white line intensity in Fig. 9(a) upon annealing in O$_2$ or H$_2$O

might also be indicative of the presence of chemisorbed oxygen, and not PtO_x, the presence of PtO_x in samples S3 and S4 is evident in the EXAFS spectra from the decrease in the Pt–Pt contribution (coordination numbers) concomitant with an increase in the Pt–O component. Fig. S8 (ESI†) shows the EXAFS spectra, fitted with Pt–Pt and Pt–O components. The fit results are shown in Table S4 (ESI†). From this analysis, the largest oxide content was obtained for S3 (O_2) followed by S4 (H_2O), while no significant Pt–O contribution was observed for S5 (H_2).

Although NP redispersion has been reported for the Pt/γ-Al_2O_3 system after annealing in oxygen at temperatures below 600 °C,[83–85] treatments at higher temperature in the same environment were shown to result in NP sintering.[83,84,86,87] Furthermore, redispersion of metal NPs was only observed for systems characterized by strong interactions between the metal oxides formed on the NPs and the oxide support. Such a phenomenon was found to involve the detachment of metal oxide species from the NPs and their subsequent migration to trap sites on the support surface. The stronger binding of PtO_x to Al_2O_3, as opposed to metallic Pt, and better wetting of the γ-Al_2O_3 surface, is expected to underlie the enhanced thermal stability of our Pt NPs after pretreatments in oxygen at temperatures below 400 °C (sample S1 as compared to S2) and also during coarsening treatment in oxygen at 450 °C (S3 as compared to S5). It should also be noted that low metal loadings and high surface area supports are crucial for this phenomenon to occur,[88] which might be related to the need of available defect sites on the support surface to stabilize the redispersed clusters. Sample annealing in reducing environments (e.g. hydrogen) or at high temperature in oxygen (above 600 °C) leads to the reduction of the oxidized metal species, the concomitant weakening of the NP/support bond, and the release of the trapped oxide species, resulting in NP sintering.[83,84,89] The latter is observed for samples S2 and S5.

In addition to enhancing the stability of the NPs against coarsening, pre-treatments in oxygen may also lead to changes in the catalytic activity and selectivity of NPs, as described by Singh et al.[90] during the oxidation of carbon monoxide and Paredis et al.[20] during the partial and total oxidation of 2-propanol.

The work described above emphasizes the importance of in situ investigations for the understanding of coarsening phenomena at the nanoscale. Furthermore, we have illustrated that EXAFS is a powerful technique for monitoring the in situ evolution of the structure and size of small NPs under real industrial operation conditions, e.g. under high temperature and in the presence of adsorbates. TEM is a great complementary technique to EXAFS for these types of studies. Nevertheless, even though significant progress has already been made in the development of environmental TEMs, studies of NPs in the size range shown here for S1 ($\sim$1 nm) at elevated temperatures (800 °C) are far from trivial, especially under a gaseous environment. Future developments in this field are expected to allow combining spectroscopic techniques such as EXAFS with microscopy techniques such as TEM within the same environmental cell, which will facilitate the determination of the coarsening mechanism and related kinetics.

5. Conclusions

We have investigated the thermal stability of inverse micelle prepared Pt nanoparticles supported on γ-Al_2O_3 and demonstrated the applicability of EXAFS as a tool for studying nanoparticle coarsening at high temperature and under gaseous environments. It is shown that different sample pretreatments lead to drastically different coarsening behaviors for two identically synthesized NP samples, with a pretreatment in O_2 leading to decreased sintering. We found that ligand-free inverse micelle prepared NPs can be stabilized against coarsening up to at least 650 °C, and that they remain relatively small ($\sim$1 nm) after annealing for several hours at 800 °C. In addition, the comparison of samples annealed at 450 °C under different chemical atmospheres corroborated that reducing environments (H_2) lead to drastic NP sintering even at moderate annealing temperatures, while slight or no coarsening was observed upon annealing in water and oxygen, respectively. The formation of PtO_x species upon O_2 annealing and the associated increase in the strength of the NP/support bond, possibly involving Pt–OH species, are considered to be possible explanations for the observed effects. Our findings might be of relevance for high temperature industrial catalysis applications, since sintered NPs with low surface-to-volume ratios have been generally shown to display decreased chemical reactivities.

References

1 B. Roldan Cuenya, *Thin Solid Films*, 2010, **518**, 3127.
2 S. J. Chen, F. C. Chien, G. Y. Lin and K. C. Lee, *Opt. Lett.*, 2004, **29**, 1390.
3 N. Nath and A. Chilkoti, *Anal. Chem.*, 2004, **76**, 5370.
4 A. P. Alivisatos, *J. Phys. Chem.*, 1996, **100**, 13226.
5 F. Tao and M. Salmeron, *Science*, 2011, **331**, 171.
6 J. O. Hansen, E. Lira, P. Galliker, J. G. Wang, P. T. Sprunger, Z. S. Li, E. Laegsgaard, S. Wendt, B. Hammer and F. Besenbacher, *J. Phys. Chem. C*, 2010, **114**, 16964.
7 D. Matthey, J. G. Wang, S. Wendt, J. Matthiesen, R. Schaub, E. Laegsgaard, B. Hammer and F. Besenbacher, *Science*, 2007, **315**, 1692.
8 M. Haruta, *Catal. Today*, 1997, **36**, 153.
9 M. Mavrikakis, P. Stoltze and J. K. Norskov, *Catal. Lett.*, 2000, **64**, 101.
10 T. V. Choudhary and D. W. Goodman, *Top. Catal.*, 2002, **21**, 25.
11 C. T. Campbell, *Science*, 2004, **306**, 234.
12 L. K. Ono, D. Sudfeld and B. Roldan Cuenya, *Surf. Sci.*, 2006, **600**, 5041.

13 J. R. Croy, S. Mostafa, J. Liu, Y. Sohn and B. Roldan Cuenya, *Catal. Lett.*, 2007, **118**, 1.

14 T. Schalow, B. Brandt, D. E. Starr, M. Laurin, S. K. Shaikhutdinov, S. Schauermann, J. Libuda and H.-J. Freund, *Phys. Chem. Chem. Phys.*, 2007, **9**, 1347.

15 H. Feng, J. A. Libera, P. C. Stair, J. T. Miller and J. W. Elam, *ACS Catal.*, 2011, **1**, 665.

16 L. K. Ono, J. R. Croy, H. Heinrich and B. Roldan Cuenya, *J. Phys. Chem. C*, 2011, **115**, 16856.

17 J. M. Flores-Camacho, J.-H. Fischer-Wolfarth, M. Peter, C. T. Campbell, S. Schauermann and H.-J. Freund, *Phys. Chem. Chem. Phys.*, 2011, **13**, 16800.

18 M. Crespo-Quesada, A. Yarulin, M. Jin, Y. Xia and L. Kiwi-Minsker, *J. Am. Chem. Soc.*, 2011, **133**, 12787.

19 K. Paredis, L. K. Ono, F. Behafarid, Z. F. Zhang, J. C. Yang, A. I. Frenkel and B. Roldan Cuenya, *J. Am. Chem. Soc.*, 2011, **133**, 13455.

20 K. Paredis, L. K. Ono, S. Mostafa, L. Li, Z. F. Zhang, J. C. Yang, L. Barrio, A. I. Frenkel and B. Roldan Cuenya, *J. Am. Chem. Soc.*, 2011, **133**, 6728.

21 G. A. Somorjai and C. J. Kliewer, *React. Kinet. Catal. Lett.*, 2009, **96**, 191.

22 H.-J. Freund, *Top. Catal.*, 2008, **48**, 137.

23 R. A. Dalla Betta, R. C. McCune and J. W. Sprys, *Ind. Eng. Chem. Prod. Res. Dev.*, 1976, **15**, 169.

24 P. J. Ferreira, G. J. la O', Y. Shao-Horn, D. Morgan, R. Makharia, S. Kocha and H. A. Gasteiger, *J. Electrochem. Soc.*, 2005, **152**, A2256.

25 G. M. Veith, A. R. Lupini, S. Rashkeev, S. J. Pennycook, D. R. Mullins, V. Schwartz, C. A. Bridges and N. J. Dudney, *J. Catal.*, 2009, **262**, 92.

26 R. S. Goeke and A. K. Datye, *Top. Catal.*, 2007, **46**, 3.

27 L. Meli and P. F. Green, *ACS Nano*, 2008, **2**, 1305.

28 H. Zhu, Z. Ma, S. H. Overbury and S. Dai, *Catal. Lett.*, 2007, **116**, 128.

29 S. Ogasawara and S. Kato, *J. Am. Chem. Soc.*, 2010, **132**, 4608.

30 O. M. Wilson, R. W. Scott, J. C. Garcia-Martinez and R. M. Crooks, *J. Am. Chem. Soc.*, 2005, **127**, 1015.

31 B. Fu, M. N. Missaghi, C. M. Downing, M. C. Kung, H. H. Kung and G. Xiao, *Chem. Mater.*, 2010, **22**, 2181.

32 M.-P. Pileni, *Nat. Mater.*, 2003, **2**, 145.

33 J. P. Gabaldon, M. Bore and A. K. Datye, *Top. Catal.*, 2007, **44**, 253.

34 S. C. Parker and C. T. Campbell, *Top. Catal.*, 2007, **44**, 3.

35 C. T. Campbell, S. C. Parker and D. E. Starr, *Science*, 2002, **317**, 44.

36 S. C. Parker and C. T. Campbell, *Phys. Rev. B*, 2007, **75**, 035430.

37 M. J. J. Jak, PhD Thesis, Leiden University, 2000.

38 M. J. J. Jak, C. Konstapel, A. Van Kreuningen, J. Chrost, J. Verhoeven and J. W. M. Frenken, *Surf. Sci.*, 2001, **474**, 28.

39 M. J. J. Jak, C. Konstapel, A. van Kreuningen, J. Verhoeven and J. W. M. Frenken, *Surf. Sci.*, 2000, **457**, 295.

40 A. El-Azab, S. Gan and Y. Liang, *Surf. Sci.*, 2002, **506**, 93.

41 O. Alexeev, D.-W. Kim, G. W. Graham, M. Shelef and B. C. Gates, *J. Catal.*, 1999, **185**, 170.

42 M. A. Newton, C. Belver-Coldeira, A. Martinez-Arias and M. Fernandez-Garcia, *Nat. Mater.*, 2007, **6**, 528.

43 B. Ingham, T. H. Lim, C. J. Dotzler, A. Henning, M. F. Toney and R. D. Tilley, *Chem. Mater.*, 2011, **23**, 3312.

44 P. J. Chupas, K. W. Chapman, G. Jennings, P. L. Lee and C. P. Grey, *J. Am. Chem. Soc.*, 2007, **129**, 13822.

45 M. A. Asoro, D. Kovar, Y. Shao-Horn, L. F. Allard and P. J. Ferreira, *Nanotechnology*, 2010, **21**, 025701.

46 L. M. Petkovic, D. M. Ginosar, H. W. Rollins, K. C. Burch, C. Deiana, H. S. Silva, M. F. Sardella and D. Granados, *Int. J. Hydrogen Energy*, 2009, **34**, 4057.

47 V. R. Choudhary, K. C. Mondal and A. S. Mamman, *J. Catal.*, 2005, **233**, 36.

48 D. M. Ginosar, H. W. Rollins, L. M. Petkovic, K. C. Burch and M. J. Rush, *Int. J. Hydrogen Energy*, 2009, **34**, 4065.

49 S. N. Rashkeev, D. M. Ginosar, L. M. Petkovic and H. H. Farrell, *Catal. Today*, 2009, **139**, 291.

50 L. M. Petkovic, D. M. Ginosar, H. W. Rollins, K. C. Burch, P. J. Pinhero and H. H. Farrell, *Appl. Catal., A*, 2008, **338**, 27.

51 P. A. Thiel, M. Shen, D.-J. Liu and J. W. Evans, *J. Phys. Chem. C*, 2009, **113**, 5047.

52 T. Hamoule, M. H. Peyrovi, M. Rashidzadeh and M. R. Toosi, *Catal. Commun.*, 2011, **16**, 234.

53 B. M. Weiss and E. Iglesia, *J. Phys. Chem. C*, 2009, **113**, 13331.

54 Y. Yamada, T. Mathew, A. Ueda, H. Shioyama and T. Kobayashi, *Appl. Surf. Sci.*, 2006, **252**, 2593.

55 Y. Oh, *Int. J. Hydrogen Energy*, 2003, **28**, 1387.

56 F. Behafarid and B. Roldan Cuenya, *Nano Lett.*, 2011, **11**, 5290.

57 S. Mostafa, F. Behafarid, J. R. Croy, L. K. Ono, L. Li, J. C. Yang, A. I. Frenkel and B. Roldan Cuenya, *J. Am. Chem. Soc.*, 2010, **132**, 15714.

58 J. R. Croy, S. Mostafa, H. Heinrich and B. Roldan Cuenya, *Catal. Lett.*, 2009, **131**, 21.

59 A. Naitabdi, F. Behafarid and B. Roldan Cuenya, *Appl. Phys. Lett.*, 2009, **94**, 083102.

60 B. Roldan Cuenya, J. R. Croy, S. Mostafa, F. Behafarid, L. Li, Z. F. Zhang, J. C. Yang, Q. Wang and A. I. Frenkel, *J. Am. Chem. Soc.*, 2010, **132**, 8747.

61 B. Ravel and M. Newville, *J. Synchrotron Radiat.*, 2005, **12**, 537.

62 M. Newville, *J. Synchrotron Radiat.*, 2001, **8**, 322.

63 B. Ravel and M. Newville, *Phys. Scr.*, 2005, **115**, 1007.

64 S. Zabinsky, J. Rehr, A. Ankudinov, R. Albers and M. Eller, *Phys. Rev. B*, 1995, **52**, 2995.

65 L.-L. Wang and D. D. Johnson, *J. Am. Chem. Soc.*, 2007, **129**, 3658.

66 E. Stern, P. Līvņš and Z. Zhang, *Phys. Rev. B*, 1991, **43**, 8850.

67 B. H. Morrow and A. Striolo, *Nanotechnology*, 2008, **19**, 195711.

68 Q. Mei and K. Lu, *Prog. Mater. Sci.*, 2007, **52**, 1175.

69 S. I. Sanchez, L. D. Menard, A. Bram, J. H. Kang, M. W. Small, R. G. Nuzzo and A. I. Frenkel, *J. Am. Chem. Soc.*, 2009, **131**, 7040.

70 A. I. Frenkel, *J. Synchrotron Radiat.*, 1999, **6**, 293.

71 B. Roldan Cuenya, A. I. Frenkel, S. Mostafa, F. Behafarid, J. R. Croy, L. K. Ono and Q. Wang, *Phys. Rev. B*, 2010, **82**, 155450.

72 J. H. Kang, L. D. Menard, R. G. Nuzzo and A. I. Frenkel, *J. Am. Chem. Soc.*, 2006, **128**, 12068.

73 W. Setthapun, W. D. Williams, S. M. Kim, H. Feng, J. W. Elam, F. A. Rabuffetti, K. R. Poeppelmeier, P. C. Stair, E. A. Stach, F. H. Ribeiro, J. T. Miller and C. L. Marshall, *J. Phys. Chem. C*, 2010, **114**, 9758.

74 M. K. Oudenhuijzen, J. H. Bitter and D. C. Koningsberger, *J. Phys. Chem. B*, 2001, **105**, 4616.

75 F. Vila, J. J. Rehr, J. Kas, R. G. Nuzzo and A. I. Frenkel, *Phys. Rev. B*, 2008, **78**, 121404.

76 A. Jentys, *Phys. Chem. Chem. Phys.*, 1999, **1**, 4059.

77 A. I. Frenkel, C. W. Hills and R. G. Nuzzo, *J. Phys. Chem. B*, 2001, **105**, 12689.

78 M. A. Brown, E. Carrasco, M. Sterrer and H.-J. Freund, *J. Am. Chem. Soc.*, 2010, **132**, 4064.

79 B. Roldan Cuenya, M. A. Ortigoza, L. K. Ono, F. Behafarid, S. Mostafa, J. R. Croy, K. Paredis, G. Shafai, T. S. Rahman, L. Li, Z. Zhang and J. C. Yang, *Phys. Rev. B*, 2011, **84**, 245438.

80 F. Behafarid and B. Roldan Cuenya, *Surf. Sci.*, 2012, **606**, 908.

81 L. K. Ono and B. Roldan Cuenya, *Catal. Lett.*, 2007, **113**, 86.

82 M. C. R. Jensen, K. Venkataramani, S. Helveg, B. S. Clausen, M. Reichling, F. Besenbacher and J. V. Lauritsen, *J. Phys. Chem. C*, 2008, **112**, 16953.

83 T. J. Lee and Y. G. Kim, *Korean J. Chem. Eng.*, 1985, **2**, 119.

84 G. I. Straguzzi, H. R. Aduriz and C. E. Gigola, *J. Catal.*, 1980, **66**, 171.

85 S. W. Weller and A. A. Montagna, *J. Catal.*, 1971, **20**, 394.

86 P. Loof, B. Stenbom, H. Norden and B. Kasemo, *J. Catal.*, 1993, **144**, 60.

87 S. B. Simonsen, I. Chorkendorff, S. Dahl, M. Skoglundh, J. Sehested and S. Helveg, *J. Am. Chem. Soc.*, 2010, **132**, 7968.

88 J. E. Stulga, P. Wynblatt and J. K. Tien, *J. Catal.*, 1980, **62**, 59.

89 E. Ruckenstein and Y. F. Chu, *J. Catal.*, 1979, **59**, 109.

90 J. Singh, E. M. C. Alayon, M. Tromp, O. V. Safonova, P. Glatzel, M. Nachtegaal, R. Frahm and J. A. van Bokhoven, *Angew. Chem., Int. Ed.*, 2008, **47**, 9260.